Carbon 235 (2025) 120086

Contents lists available at ScienceDirect

Carbon

journal homepage: www.elsevier.com/locate/carbon

Vertically aligned carbon nanotubes from premade binary metal oxide nanoparticles on bare SiO_2

Abdul Hoque, Chaminda P. Nawarathne, Noe T. Alvarez *

Department of Chemistry, University of Cincinnati, Cincinnati, OH, 45221, United States

A B S T R A C T

The synthesis of carbon nanotubes (CNTs) requires well-defined catalyst nanoparticles that can influence both diameter and chirality. Herein, catalyst nanoparticles containing both the catalyst and catalyst support material were developed. Binary-metal oxide (AlO_x–Fe_2O_3) nanoparticles was synthesized from a mixture containing both aluminum and iron oleate precursors in the solution phase. The nanoparticles were assembled as a monolayer film on a silicon oxide (SiO_2) substrate via organic linker molecules to synthesize vertically aligned carbon nanotubes (VA-CNTs). Microscopic and spectroscopic characterization of the premade catalyst nanoparticles and monolayer film assembly revealed the quality of the nanoscale assembly, which facilitated the successful growth of VA-CNTs. The length of the CNTs synthesized using these AlO_x–Fe_2O_3 nanorice catalyst nanoparticles surpassed that of previously reported CNTs grown on bare SiO_2 surfaces without oxide buffer layers. In addition, the CNTs appeared to be directly bonded/connected to the SiO_2 substrate, suggesting CNT formation via the tip-growth mechanism. The effects of growth temperature and catalyst reduction time were evaluated to obtain high-yield VA-CNTs.

1. Introduction

Carbon nanotubes (CNTs) are important materials for developing electrically conducting fibers [1], nanoscale electronics, biosensors [2], and energy storage devices [3,4]. The optical, mechanical, and electronic properties of CNTs are influenced by their structural properties, such as diameter and chirality. While few-walled (3–10) CNTs are valuable because of their unique physical properties such as enhanced mechanical strength [5,6], semiconducting single-walled CNTs have additional optical properties and they have employed in the fabrication of chemical/biosensors for molecular electronics, field-effect transistors, and optoelectronic devices [7–9]. Vertically aligned CNTs (VA-CNTs) can be assembled into electrically conducting fibers or ribbons [10,11]. The excellent mechanical strength of CNTs makes them suitable for building superstrong fibers, ballistic armor, and even the space elevator [12]. CNTs are often used to fabricate composite materials with improved mechanical properties, and longer CNTs have shown increased mechanical strength and electrical conductivity [13,14].

Chemical vapor deposition (CVD) is the preferred method for large-scale synthesis of VA-CNT arrays, with catalyst engineering on the substrate being crucial for success. High nanoparticle density on the substrate can affect the length, direction, and density of nanotubes [15,16]. The most common method for preparing catalyst and catalyst supports is through thin-film formation using physical vapor deposition (PVD) or CVD techniques, such as sputtering, e-beam deposition, or atomic layer deposition [17]. Thermal annealing of this catalyst thin films convert into nanoparticles for CNT growth. However, controlling the homogeneity and size of these catalyst nanoparticles is challenging. Additionally, thin-film catalysts may form intermetallic compounds at high temperatures, reducing the CNT growth rates by decreasing carbon consumption [18]. In addition, the techniques used for preparing thin-film catalysts are expensive because of the high vacuum conditions required and maintenance costs. Solution-based metal precursors have also been used to form catalyst particles in situ through mist deposition [19], and thermal evaporation [20,21] in order to make the synthesis process less expensive. Premade catalyst nanoparticles that are synthesized in the solution phase and then assembled onto a substrate for VA-CNT growth provide an alternative for more size and composition control for scalable high-density CNT growth [22–24]. Compared with PVD thin-film catalyst preparation, this solution-phase process is advantageous in terms of cost and potentially controlling the size and homogeneity, monodispersity, and particle density.

An essential element for VA-CNT synthesis via CVD is the oxide-film catalyst support placed between the catalyst and silicon oxide (SiO_2) substrate. Diverse forms of Al-oxides have shown to produces small, narrower size-distribution catalyst nanoparticles, likely due to their higher acidity of alumina (Al_2O_3) [25]. As a catalyst support, Al_2O_3 can reduce the surface diffusion and ripening of metal catalysts to grow VA-CNTs [17,26]. Additionally, Al_2O_3 has an important carbon cracking ability, enhancing the decomposition of carbon precursors and

* Corresponding author.
E-mail address: alvarene@ucmail.uc.edu (N.T. Alvarez).

https://doi.org/10.1016/j.carbon.2025.120086
Received 7 December 2024; Received in revised form 27 January 2025; Accepted 2 February 2025
Available online 3 February 2025

accelerating CNT growth kinetics [27]. Furthermore, synthesis of long and good quality of VA-CNTs on bare SiO_2 (without an Al_2O_3 buffer layer) is challenging due to the catalyst particle aggregation, metal ion diffusion and silicate formations. Typical growth rates of 15 μm/h have been observed in SiO_2 substrates [28], while complex patterning in these substrates has only achieved CNT lengths of tens of microns. In contrast, Al_2O_3 substrates typically yield CNT lengths in the hundreds of microns [29]. Catalyst ripening and subsurface diffusion on SiO_2 reduce the particles density, impacting VA-CNT growth. The properties of SiO_2-supported iron, such as acidity, reducibility, and size distribution, differ from those of Al_2O_3-supported iron. Iron dispersion, which determines the size of the particles formed on both substrates, is greater on Al_2O_3 surfaces than on SiO_2 surfaces [25]. Without a catalyst support, VA-CNTs synthesized on SiO_2 are larger in diameter, randomly oriented and short [7,30,31]. Our previous work indicated that shorter VA-CNT grow on SiO_2 substrates without an Al_2O_3 support, whereas the VA-CNT length increases with a catalyst support [24,32]. Therefore, an Al_2O_3 catalyst support on the SiO_2 substrate is crucial for growing high-density, long VA-CNTs. While PVD and CVD are commonly used to prepare Al_2O_3 thin films as catalyst supports, there is limited research on wet-chemistry-based methods for synthesizing VA-CNTs [24,33].

In this study, catalyst nanoparticles known as nanorice, which include both the active catalyst component Fe and its support (AlO_x), were employed for the synthesis of VA-CNTs on bare SiO_2 substrates. These binary metal oxide (AlO_x–Fe_2O_3) nanorice particles were synthesized via the thermal decomposition method, and a monolayer thin film of nanoparticles was assembled on the SiO_2 substrate using bifunctional organic linker molecules. This setup was then utilized for the growth of VA-CNTs at different temperatures using traditional CVD methods. The developed wet-chemistry-based approach shows promise as a simple and cost-effective method for preparing catalysts for the growth of VA-CNTs. An important objective of this approach is to dismiss the use of Al_2O_3 thin films employed as catalyst support for the growth of VA-CNTs.

2. Experimental

2.1. Materials

Aluminum chloride (ReagentPlus grade, ≥99 %), iron(III) chloride hexahydrate (reagent grade, ≥98 %), oleic acid (technical grade, ≥90 %), and 11-phosphonoundecanoic acid (PNDA; ≥90 %) were purchased from Sigma-Aldrich (St. Louis, MO, USA) and used without further purification. Sodium oleate (≥97.0 %) was purchased from TCI Chemicals (Tokyo, Japan). Hexanes (ACS grade, ≥99.5 %), 1-octanol (≥98 %), and ethanol (ACS grade) were purchased from Fischer Scientific (Waltham, MA, USA). Ultrathin carbon type-A 400 mesh copper grids for transmission electron microscopy (TEM) characterization were obtained from Ted Pella (Redding, CA, USA). Single-side-mirror-polished SiO_2 wafers were purchased from University Wafer (Boston, MA, USA). Ultrahigh-purity hydrogen (99.99 %), high-purity acetylene (99.99 %), and liquid argon gas were purchased from Wright Brothers, Inc. (Ohio, USA).

2.2. Catalyst synthesis

The AlO_x–Fe_2O_3 nanorice was synthesized following our previously reported procedure [34]. A mixture of iron oleate and aluminum oleate precursors was used in the thermal decomposition reaction to form binary metal oxide nanoparticles. Iron oleate and aluminum oleate complexes were synthesized separately using ferric chloride and aluminum chloride salts according to the procedures reported by Park et al. [35] and Hoque et al. [36], respectively. A mixture of 1.0 g of iron oleate and 5.0 g of aluminum oleate complexes were dissolved in 50 mL of 1-octanol with 4.5 mL of oleic acid as a stabilizing agent. The precursor mixture was then heated at 100 °C for 30 min to dissolve the precursors completely. After increasing the temperature to 195 °C, the reaction was allowed to proceed for 30 min to promote AlO_x–Fe_2O_3 nanorice formation. The solution was cooled to room temperature and the nanorice particles were collected by a centrifugation at 15,000 rpm for 90 min. Purification was performed by dispersing the obtained particles in hexane and washing twice. Purified AlO_x–Fe_2O_3 nanorice was stored in hexane until further use.

2.3. Substrate functionalization and monolayer film assembly

A 25.4 × 25.4 mm^2 SiO_2 wafer was employed as a substrate for the synthesis of VA-CNTs using a AlO_x–Fe_2O_3 nanorice monolayer film. To assemble a monolayer of AlO_x–Fe_2O_3 nanorice on the SiO_2 substrate, PNDA, a bifunctional organic linker, was coupled to the hydroxylated SiO_2 surface using a previously reported method with some modifications [24,37]. First, the substrate surface was activated with hydroxyl (–OH) groups to aid in forming hydrogen bonds with the phosphonic acid functional groups of the crosslinking molecules. After the SiO_2 substrate was cleaned by ultrasonication in acetone for 20 min, the polished side was hydroxylated using piranha solution (H_2SO_4:H_2O_2, 3:1) for 30 min [38]. Phosphonate groups have higher affinity for metal oxide substrates than carboxylate group [39]. Therefore, when the hydroxylated SiO_2 substrate was immersed in a 1 mM PNDA solution (ethanol:water, 1:1, v/v), the PNDA ligands were attached to the SiO_2 surface via hydrogen bonding with the phosphonate group, resulting in a terminal carboxylate group. X-ray photoelectron spectroscopy (XPS) was used confirm the binding of phosphonate to the SiO_2 surface. Subsequently, the substrate was washed with a mixture of pure ethanol and water. The PNDA-functionalized SiO_2 substrate was placed in a 3.0 mg/mL oleic acid-coated AlO_x–Fe_2O_3 nanorice solution for 3 h, and the carboxylate group of oleic acid on the AlO_x–Fe_2O_3 nanorice surface underwent ligand exchange with the terminal carboxylate of PNDA. Thus, this linker molecule anchored the nanorice on the SiO_2 substrate to form a monolayer of nanoparticles [37].

2.4. VA-CNT growth

VA-CNTs were synthesized using traditional thermal CVD technique, in which the AlO_x–Fe_2O_3 nanorice monolayer film on the SiO_2 substrate was employed as a catalyst. The schematic illustration in Fig. 1 shows the steps for monolayer formation and VA-CNT growth. Prior to the growth process, the nanorice monolayer on the substrate was annealed in open air for 4 h at 360 °C to remove oleic acid from the nanoparticle surfaces. VA-CNT synthesis was performed using acetylene as the hydrocarbon source at a rate of 100 sccm, with H_2 (300 sccm) and Ar (1000 sccm) as carrier gases at atmospheric pressure. As the premade AlO_x–Fe_2O_3 nanorice was in the oxide form, the Fe_2O_3 catalyst was reduced at 450 °C for 3 min using H_2 as a reducing agent to convert from the oxide to the metallic form. The synthesis of VA-CNTs using the monolayer catalyst was conducted at three different temperatures (670, 720, and 750 °C). Subsequently, the high-temperature furnace was cooled to 150 °C under an argon environment to prevent VA-CNT oxidation.

2.5. Characterization

The size distribution of the AlO_x–Fe_2O_3 nanorice was measured using atomic force microscopy (AFM; Dimension Icon ScanAsyst, Bruker, Billerica, MA, USA) in noncontact tapping mode with a scan rate of 1 Hz and a resolution of 512 × 512 pixels. The AFM sample for particle size measurement was prepared by spin coating a drop of nanoparticle solution on a single-side-mirror-polished SiO_2 substrate that creates a sparse low particle concentration. After washing with hexane, the samples were annealed at 100 °C to remove solvent from the surface. The shape of the catalyst nanoparticle was investigated by FEI Talos F200X transmission electron microscopy (TEM; Thermo Scientific,

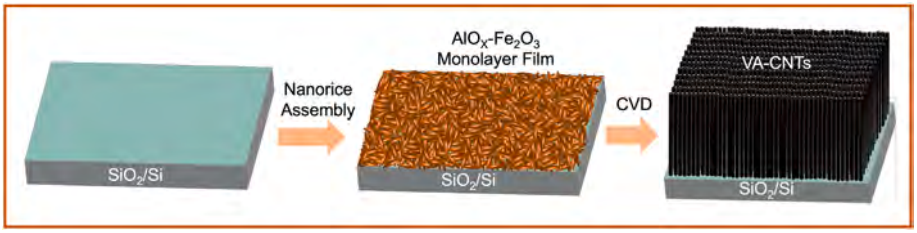

Fig. 1. Schematic illustration of the AlO_x–Fe_2O_3 nanorice assembly on a SiO_2 substrate for VA-CNT synthesis.

Waltham, MA, USA) at 200 kV and the high-angle annular dark-field (HAADF) STEM images were collected using Super-X EDAX analytical system connected with the same instrument. For TEM sample preparation of CNT, a small piece of array was dispersed in ethanol and sonicated for 2 min to obtain a homogeneous dispersion. One drop of the CNT dispersion was drop casted on a TEM grid, which was then annealed at 70 °C for 24 h to remove solvent from the grid. The crystallinities of the as-synthesized and annealed AlO_x–Fe_2O_3 nanoparticles were studied using X-ray diffraction (XRD; X'pert multipurpose diffractometer, PANalytical, Almelo, Netherlands) with a Cu K_α ($\lambda = 1.54056$ Å) source operated at 40 mA and 45 kV. XPS characterization was performed using a K-Alpha X-ray photoelectron spectrometer (Thermo Scientific, Waltham, MA, USA) with an Al Kα micro-focused monochromator and a 128 channel detection system. XPS spectra were collected using a spot size of 400 μm and 10 cycles. The XPS spectra were analyzed using Avantage software (version 5.9918) to determine the content (at%) of each species. XPS data acquisition and analysis were performed using OriginPro 8.5 software. First, all the XPS core-level peaks were calibrated using the C 1s peak at 284.8 eV to correct for charging effects. Then, the XPS peaks were fitted using Gaussian components after background subtraction. The binding energies of different elements were obtained by comparing the experimental results with the NIST XPS Database and relevant literature. Scanning electron microscopy (SEM) micrographs were recorded using an FEI Apreo SEM (Thermo Fisher Scientific, Waltham, MA, USA) at acceleration voltages of 5–10 kV and a current of 0.2 nA with working distance of ~10 mm. Energy-dispersive X-ray analysis (EDAX) for the elemental composition of nanorice was performed using the same instrument. The quality of the synthesized VA-CNTs was investigated by Raman spectroscopy using an inVia™ confocal Raman microscope (Renishaw, Gluocestershire, UK) with a 633 nm laser at 10 % power.

3. Results and discussion

The main advantage of the AlO_x–Fe_2O_3 nanorice catalyst is that the catalyst support (AlO_x) and active catalyst (Fe_2O_3) component are

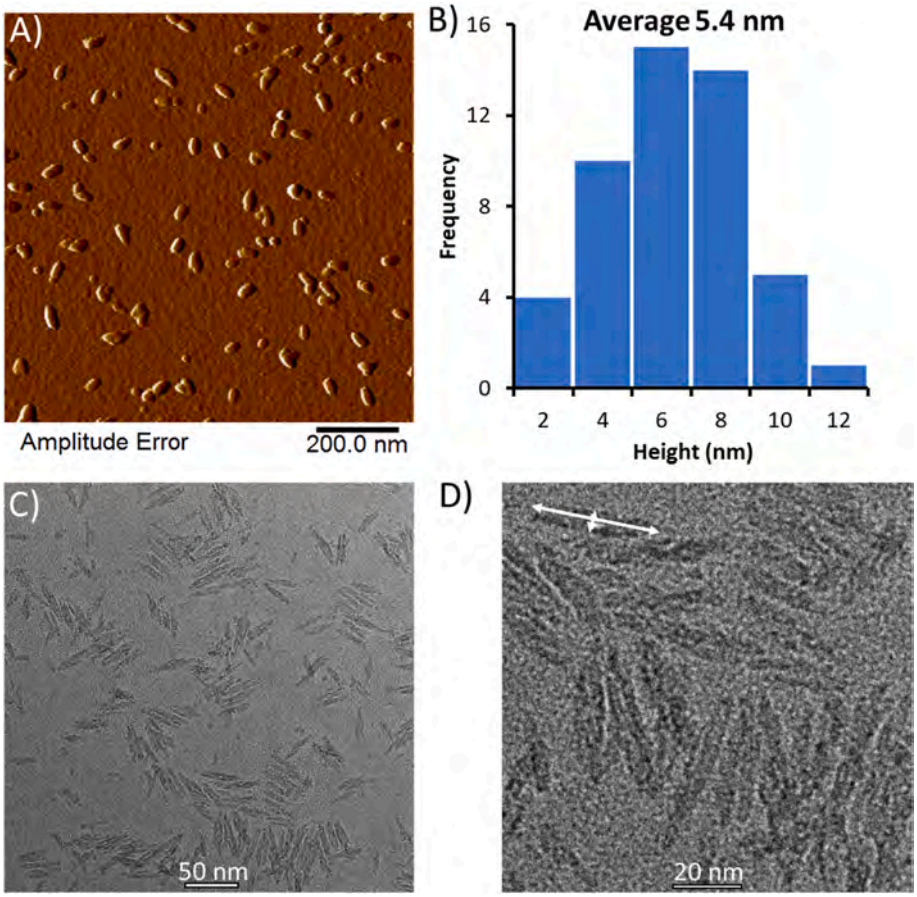

Fig. 2. AFM and TEM images of AlO_x–Fe_2O_3 nanorice particles. (A) AFM image of nanorice particles on the SiO_2 substrate, (B) height distribution of AlO_x–Fe_2O_3 nanorice particles collected from height sensor AFM images, and (C) low-magnification and (D) high-magnification TEM images of AlO_x–Fe_2O_3 nanorice particles.

combined in the same particle; therefore, an extra catalyst support layer is not necessary for VA-CNT synthesis. Moreover, the premade nanorice particles eliminate the need for expensive instrumentation for catalyst deposition. The AlO_x–Fe_2O_3 nanorice catalyst was prepared from a mixture of aluminum oleate and iron oleate precursors via a thermal decomposition reaction [34]. AFM and TEM analysis revealed that the as-synthesized AlO_x–Fe_2O_3 nanoparticles had rice-shaped structures with a known composition and relatively small size distribution (Fig. 2). In particular, the particle size distribution obtained by AFM characterization (Fig. 2B) gave an average height of 5.4 nm, which corresponds to the width of a nanorice particle. The low-magnification (Fig. 2C) and high-magnification (Fig. 2D) TEM images of the AlO_x–Fe_2O_3 nanorice show an identical particle structures. The white arrows in the high-magnification TEM image (Fig. 2D) indicate that the rice-shaped particles have a length of approximately 38 nm, whereas the width is only 6.6 nm, consistent the AFM results.

The elemental composition of the AlO_x–Fe_2O_3 nanorice on the SiO_2 substrate was confirmed using EDAX, as detailed in the supplementary information section. The EDAX results (Fig. S1B) collected from the SEM image (Fig. S1A) of the AlO_x–Fe_2O_3 nanorice indicate the presence of Al, Fe, and O. The large peak in the EDAX spectrum corresponds to Si, which originates from the SiO_2 substrate used for SEM sample preparation. As a 5:1 atomic ratio of aluminum oleate and iron oleate precursors was used to synthesize the AlO_x–Fe_2O_3 nanorice, the weight percentage of Al (60.67 %) is higher than that of Fe (8.49 %). The weight percentage of oxygen present in the sample is 30.84 %, which might be influenced by the SiO_2 substrate used for sample preparation.

We further characterized the AlO_x–Fe_2O_3 nanorice particles via elemental mapping, XPS, and XRD (Fig. S2) to obtain a better understanding of their chemical composition, oxidation states, and crystalline structures. The HAADF-STEM image (Fig. S2A) image of the AlO_x–Fe_2O_3 nanorice and corresponding elemental mapping indicate the presence of Al, Fe, and O in the particles. XPS is a versatile characterization technique for studying the composition and chemical states of the elements present on the surface of nanomaterials. The XPS survey spectrum and core-level spectra (Fig. S2B) of the AlO_x–Fe_2O_3 nanorice (Fig. S2B) show the presence of Al 2p, Fe 2p, O 1s, and C 1s in the sample. The peak at a binding energy ~75.0 eV indicates the presence of AlO_x in the particles. The deconvoluted O 1s core-level spectrum has two peaks that represent Al–OH (~532 eV) and Al–O (~530.8 eV) bonds in the molecular structure. The –OH groups could originate from surface-adsorbed H_2O or surface hydroxides of AlO_x or Fe_2O_3. The Fe 2p core-level spectrum exhibits Fe $2p_{1/2}$ and Fe $2p_{3/2}$ peaks along with their corresponding satellite peaks in the range of 708–738 eV. The Fe $2p_{1/2}$ and Fe $2p_{3/2}$ peak positions assist to the identification of the chemical state and environment of Fe on the sample surface [40]. The binding energies of Fe $2p_{1/2}$ and Fe $2p_{3/2}$ in the AlO_x–Fe_2O_3 nanorice are 724.5 and 711 eV, respectively. In the C 1s core-level spectrum, the peak at 284.8 eV indicates the presence of sp^3 carbon, whereas those at ~286.4 and ~288.5 eV correspond to C–O and O–C═O surface functional groups, indicating the presence of oleic acid on the surface of the AlO_x–Fe_2O_3 nanorice [41].

The amorphous or crystalline nature of the as-synthesized AlO_x–Fe_2O_3 nanorice as well as the samples annealed at 700 and 1100 °C was characterized using XRD (Fig. S3). Crystalline α-Fe_2O_3 and amorphous AlO_x are present in the as-synthesized nanoparticles, whereas the nanorice particles are converted from amorphous AlO_x into γ-Al_2O_3 and α-Al_2O_3 after heat treatment inn open air at 700 and 1100 °C, respectively.

Monolayer assembly of the catalyst nanorice particles on the SiO_2 substrate was achieved using bifunctional linker molecules according to a previously reported procedure [24,36]. The SiO_2 substrate was functionalized with PNDA, which acted as a linker to anchor the nanoparticles, with the phosphonate group interacting with the substrate surface and the terminal carboxylic group binding to the surface of the AlO_x–Fe_2O_3 nanorice. Successful functionalization of the SiO_2 substrate with PNDA was verified using XPS (Fig. S4). A comparison of the XPS survey spectra of the bare and PNDA-functionalized SiO_2 substrates reveals the presence of phosphorus (P 2s and P 2p) on the latter surface (Fig. S4A). In the P 2p core-level spectrum (Fig. S4B), the peak at 132.9 eV confirms that the phosphonate groups are bonded to the SiO_2 substrate (Fig. S4A). A monolayer film of AlO_x–Fe_2O_3 nanorice was formed on the SiO_2 substrate via a ligand exchange reaction. The carboxylate group of the PNDA linker replaces the carboxylate group of oleic acid on the surface of the AlO_x–Fe_2O_3 nanorice, resulting in the formation a monolayer film on the substrate surface. The formation of this catalyst monolayer on SiO_2 is key for controlling VA-CNT growth because it eliminates the nucleation of multiple nanotubes at the same location on the substrate. Monolayer formation allows the positioning of nanoparticles next to each other, thereby creating a sufficient nucleation density to support the growth of VA-CNTs. In addition, this approach eliminates the possibility of excess active catalyst nanoparticles, which can induce a lack of continuity between the CNTs at the bottom and top of the array. Furthermore, this monolayer of catalyst nanoparticles would allow carbide formation between C atoms on the CNTs and Si atoms on the SiO_2 surface.

The surface morphologies of the bare and monolayer-functionalized substrate were characterized using AFM and SEM (Fig. 3). The AFM images of the bare substrate (Fig. 3A and B) and monolayer-functionalized substrate (Fig. 3C and D) reveal differences in the surface morphology before and after formation of the nanoparticle monolayer film. The amplitude error (Fig. 3A) and height sensor (Fig. 3B) AFM images of the bare SiO_2 substrate show a smooth surface morphology with no particles. In contrast, the AFM images of the monolayer film of AlO_x–Fe_2O_3 nanorice (Fig. 3C and D) reveal a uniform layer of high-density particles on the surface.

Such high-density catalyst particle in a monolayer format for VACNTs growth was achieved through ligand exchange reactions between the SiO_2 substrate surface and the catalyst nanorice surface oxide. This monolayer formation strategy has been discussed in several literature publications, including previous work from our group [24,36], where PNDA linkers are employed for the temporary fixation of nanoparticles on substrates via ligan exchange reactions. Given the nanoscale size of the catalyst nanoparticles, it is ideal to pack them densely on the substrate in order to support the synthesis of VACNTs. According to current literature, a density of 10^9 to 10^{12} catalyst nanoparticles per square centimeter is required to grow VACNTs [42]. Our calculations show that the nanorice particle density onto silicon oxide substrate is 8.75 x 10^{10} per square cm (AFM image, Fig. 3D), indicating that the monolayer assembly is suitable for growing VACNTs.

The morphology of the AlO_x–Fe_2O_3 nanorice monolayer on the SiO_2 substrate was also characterized using SEM. The low-magnification (Fig. 3E) and high-magnification (Fig. 3F) SEM images of the AlO_x–Fe_2O_3 nanorice monolayer film on the SiO_2 substrate indicate the narrow size distribution of these particles on the surface. This approach departs from traditional techniques, such as spin coating, drop casting, and dip coating, which cannot guarantee catalyst monolayer formation to enhance the density of the grown CNTs and the quality of the VA-CNTs.

VA-CNT synthesis was conducted via CVD using acetylene as a carbon source at three different temperatures (670, 720, and 750 °C). Thermal reduction at 450 °C was performed under flowing H_2 (400 sccm) to reduce the oxide catalyst to its metallic form. At high temperatures, hydrogen gas has been extensively employed as reducing agent and has shown to decompose into atomic hydrogen on metal catalyst surfaces [43,44], thereby promoting the reduction of metal oxides to the metallic phase, which is critical for the catalytic activity of the nanoparticles [45]. The binary metal oxide nature of the catalyst may play an important role during CNT growth due to the separation of the metal components during CNT synthesis that would potentially extend the life of catalyst nanoparticles. Fe, the active catalyst component would be bonded to the CNT while the non-active AlOx would

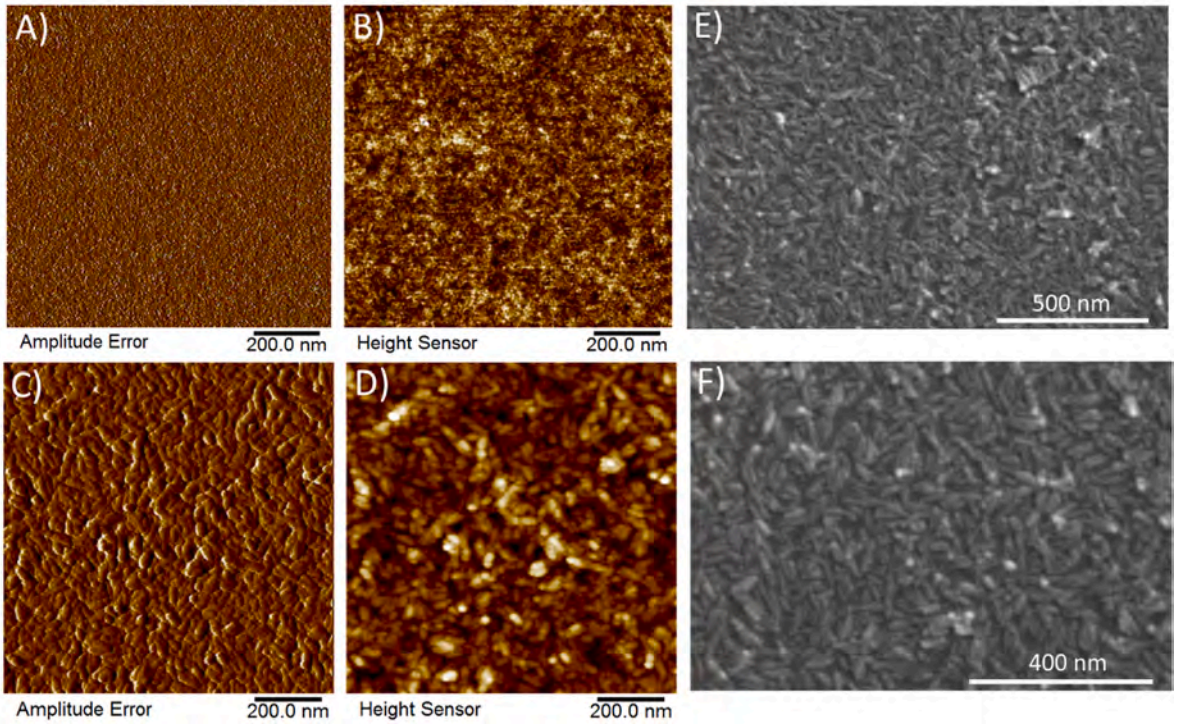

Fig. 3. AFM and SEM images of the monolayer film of AlO_x–Fe_2O_3 nanorice on the SiO_2 substrate. (A, B) Amplitude and height sensor AFM images of bare SiO_2, (C, D) AFM images of the AlO_x–Fe_2O_3 nanorice film on the SiO_2 substrate, and (E, F) low-magnification and high-magnification SEM images of the AlO_x–Fe_2O_3 nanorice monolayer.

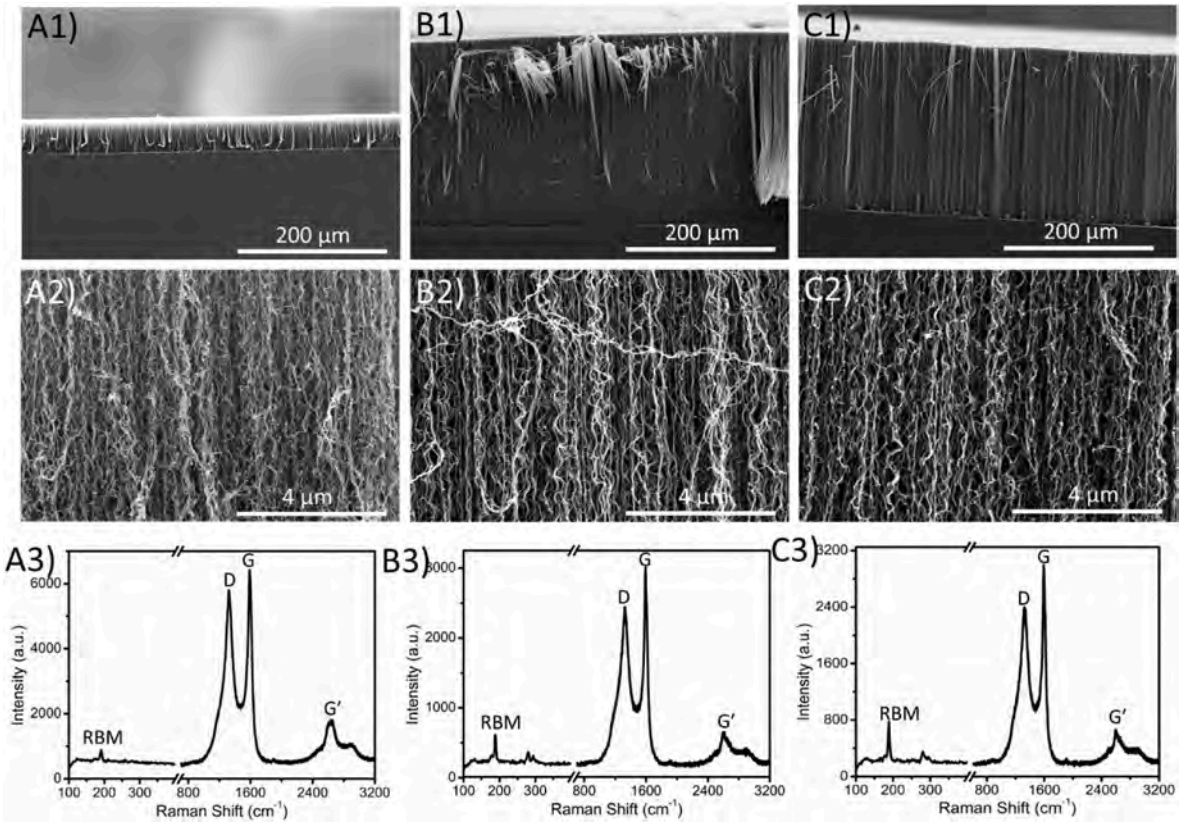

Fig. 4. SEM images of VA-CNTs synthesized using the binary metal AlO_x–Fe_2O_3 nanorice on a SiO_2 substrate at 670, 720, and 750 °C, respectively. (A1, B1, C1) Low-magnification SEM images, (A2, B2, C2) high-magnification SEM images, and (A3, B3, C3) Raman spectra of the synthesized VA-CNTs.

move away from the CNT. A theoretical work studied similar type of separation during growth of active and less-active components for bimetallic catalyst nanoparticles. They found that the more active metal component of the catalyst become separated from the less active components, where C atoms interacting with the less-active component move towards the CNT increasing CNT bonding on their model, which resulted in faster CNT growth [46].

VA-CNTs were grown using a conventional CVD technique at atmospheric pressure. Among CNT synthesis methods, CVD can achieve the large-scale production of highly pure CNTs at low temperatures [47]. A few of the CNT synthesis parameters were varied, while keeping the synthesis time (20 min) and pressure (760 Torr) constant, to evaluate the catalytic activity of the AlO_x–Fe_2O_3 nanoparticles and the characteristics of the corresponding CNTs. The SEM images in Fig. 4A1, B1, and C1, which show low-magnification side views of the obtained VA-CNTs, reveal that heights of 43, 262, and 237 μm were obtained at growth temperatures of 670, 720, and 750 °C, respectively. Thus, the longest CNTs (262 μm) were achieved at 720 °C and the shortest (43 μm) at 670 °C, indicating that the catalytic activity of the nanoparticles is temperature dependent.

Although VA-CNT synthesis using the AlO_x–Fe_2O_3 nanorice particles was relatively facile, the alignment of the CNTs within the arrays requires improvement. The high-magnification SEM images of the VA-CNTs obtained at the three growth temperatures (Fig. 4A2, B2, C2) show the alignment. Notably, longer CNTs were obtained with more homogenous nanoparticle assemblies in the monolayer. The calculated weight density of VACNTs grown from nanorice catalyst is 1.7 g/cm^3, although at the higher end, agrees with the literature density (1.58–1.90 g/cm^3) [48]. To understand well about the catalyst performance, we have also calculated the area density of carbon nanotube on the substrate using imageJ software which is 6.25 x 10^{10} per cm^2 indicating around 71 % of nanorice catalyst participated in the CNTs formation. In addition, the quality of the VA-CNTs grown with the binary metal AlO_x–Fe_2O_3 nanorice monolayer film was evaluated using the I_D/I_G ratios in Raman spectroscopy. The Raman spectra of the CNTs grown at different temperatures are shown in Fig. 4A3, B3, and C3. The G band near 1590 cm^{-1}, known as the graphitic peak, results from sp^2 C=C bond vibrations [49]. At the highest temperature (750 °C), the intensity of the G band increases relative to that of the D band near 1350 cm^{-1}. The intensity ratio of the D and G bands (I_D/I_G), which is commonly employed to define the purity and quality of CNTs [50,51], had values of 0.99, 0.80, and 0.77 at 670, 720, and 750 °C, respectively. Thus, better quality, or fewer amorphous carbon contaminants, was observed at the growth temperature of 750 °C. This behavior is consistent with previous findings that CNTs become more amorphous (less crystalline) at low temperatures and highly crystalline CNTs can be obtained using high-temperature growth [52]. Furthermore, a single radial breathing mode (RBM) peak was observed at ~170 cm^{-1}, which typically used as a signature for single-walled CNTs. The intensity of the RBM peak increased as the growth temperature increased, with a sharper, larger peak observed at 720 °C. The sharp peak in the RBM region could indicate the presence of single-walled CNTs with a diameter of ~1.4 nm or could be associated with the synthesis of a helical CNT structure according to Park et al. [53].

The growth temperature mainly depends on the type of substrate used during CVD process. Previous studies indicate that the growth temperature for CNT synthesis using premade catalyst nanoparticles is in the range of 650–800 °C (Table 1). The CVD reaction conditions should be optimized in terms of the substrate, catalyst nanoparticles, and carbon precursors used for CNT synthesis. The optimal concentrations of hydrocarbon and hydrogen gases (Table 1) can play a crucial role in producing CNTs in high yields. The length of the VA-CNTs grown using the AlO_x–Fe_2O_3 nanorice monolayer was maximized at 720 °C on the SiO_2 substrate using acetylene as a hydrocarbon source (Fig. 4B1).

The diameter distributions of the VA-CNTs synthesized at different growth temperatures were analyzed using TEM, as shown in Fig. 5. The TEM images indicate that the CNTs grown using the AlO_x–Fe_2O_3 nanorice monolayer film on the SiO_2 substrate at different temperatures have similar number of walls and diameter distributions. In contrast, owing to limited control over the size of catalyst particles, CNTs grown using thin-film catalysts exhibit different diameters. The common techniques for catalyst particle deposition on a substrate using premade nanoparticles, such as drop casting or spin coating, provide less uniform particle distributions over the surface, thereby producing CNTs with comparatively large diameters. Self-assembled monolayers of premade catalyst nanoparticles have the advantage of producing diameter-controlled VA-CNTs [58]. To calculate the average diameters of the CNTs, ImageJ software was used to analyze the collected TEM images of CNTs grown at 670, 720, and 750 °C. The calculated diameters of the CNTs grown at 720 and 750 °C are 5.9 and 5.4 nm, respectively (Fig. 5B2, C2), which is similar to the size of the catalyst. In contrast, the CNTs grown at 670 °C have a slightly larger diameter of 6.2 nm (Fig. 5 A2).

High-resolution TEM (HRTEM) was used to investigate the average number of walls in the CNTs synthesized using the AlO_x–Fe_2O_3 nanorice catalyst at different temperatures (Fig. S5). To calculate the average number of walls in the CNTs, more than 20 nanotubes were analyzed, and a histogram was constructed (Fig. S5). The CNTs grown at 720 and 750 °C have an average of four walls, whereas the CNTs with a larger diameter grown at the lower temperature of 670 °C have an average of six walls.

CNTs synthesized using the CVD process can follow two different growth mechanisms: base growth, where the catalyst particles remain on the substrate, or tip growth, where catalyst particles move toward the tips of the CNTs. The mode of CNT growth depends on the adhesion of the catalyst particles on the substrate [59]. SEM and TEM characterization was performed to confirm the position of the catalyst particles in the CNTs synthesized using the AlO_x–Fe_2O_3 nanorice monolayer film on the SiO_2 substrate. The low-magnification TEM image of the CNTs grown at 750 °C (Fig. 6A) show catalyst particles at the ends of the CNTs, even though some open-ended CNTs are observed. It is worth to mention that these CNTs were dispersed in ethanol for TEM sample preparation, therefore both ends of CNTs are expected to be seen. Higher-magnification TEM images (Fig. 6B–D) also reveal catalyst particles located on the tips of the CNTs. Catalyst particles were also observed at the tips of the CNTs in VA-CNT arrays, as shown by the TEM images at various magnifications in Figs. S6A–C. The high-magnification TEM image of the top of the CNT bundle (Fig. S6C) indicates that many catalyst particles are located at the top-end of CNTs, thereby suggesting the occurrence of tip-growth synthesis. Although the exact reason for catalyst particle detachment from the substrate remains elusive, we

Table 1
Specific CVD parameters used for the synthesis of VA-CNTs from premade nanoparticle catalysts.

Premade Catalyst	Hydrocarbon Source	Growth Temp. (°C)	H_2 Con. (sccm)	CNT Type	Ref.
Fe_3O_4 nanoparticles	Acetylene	750	400	Multiwalled	Hoque et al. [24]
Co nanoparticles	Ethanol	650, 700, 750, 800	3 %	Single walled, multiwalled	Cui et al. [54]
$CoFe_2O_4$, Fe_3O_4 nanoparticles	Acetylene	750	4 %	Multiwalled	Sato et al. [55]
Fe/Fe_3O_4 nanoparticles	Methane	650	80	Multiwalled	Baliyan et al. [56]
Fe_3O_4 nanoparticles	Ethylene	800		Multiwalled	Beard et al. [57]
$AlFe_2O_4$, Fe_3O_4 nanoparticles	Acetylene	750	210	Multiwalled	Lee et al. [23]
Fe_3O_4 nanoparticles	Acetylene	750	400	Multiwalled	Alvarez et al. [22]

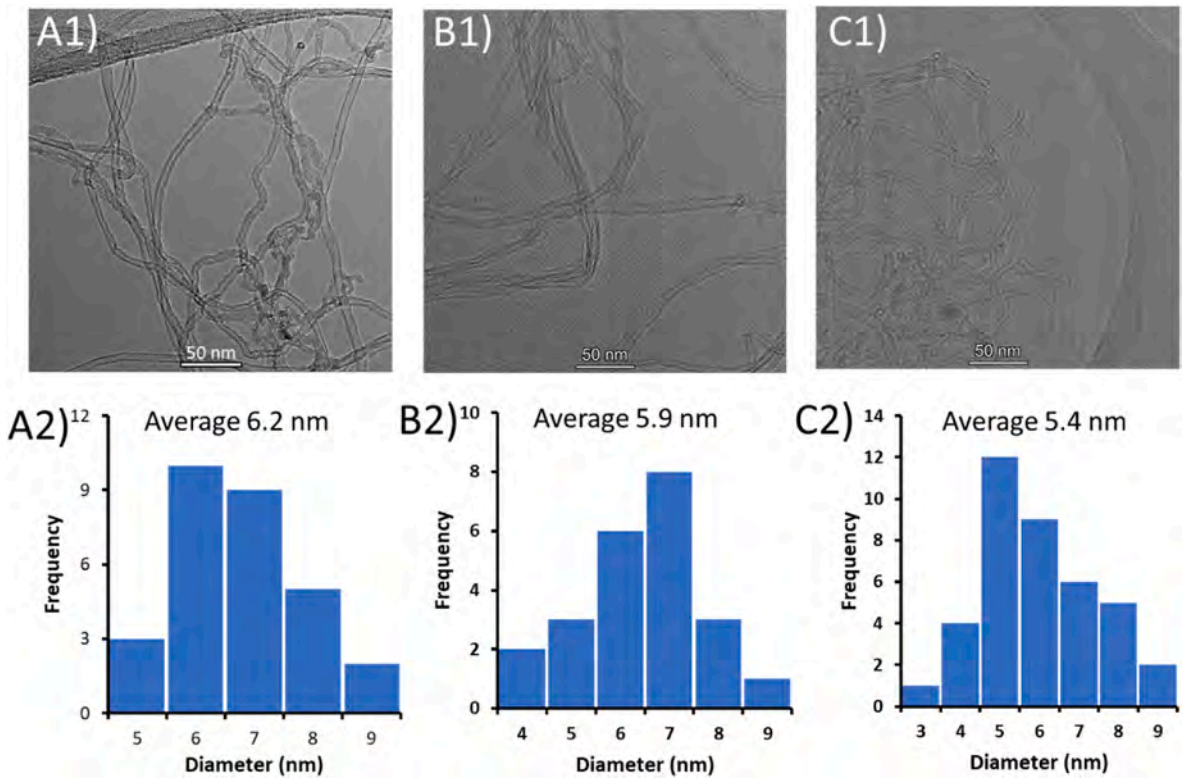

Fig. 5. TEM images of VA-CNTs synthesized using the binary metal AlO_x–Fe_2O_3 nanorice on a SiO_2 substrate and corresponding diameter distributions. (A1, B1, C1) TEM images and (A2, B2, C2) diameter distributions of the CNTs synthesized at 670, 720, and 750 °C, respectively.

suspect that the binary metal oxide catalyst undergoes phase separation at high temperatures, with some aluminum oxide remaining on the substrate and iron moving to the CNT tips. However, this behavior is inconsistent with the fact that the CNTs appear to be connected to the SiO_2 substrate, as discussed vide infra.

Furthermore, SEM analysis of the bottom part of a CNT array was performed after forcefully removing the CNTs using forceps. The high-magnification SEM image (Fig. 7B) of the CNT array grown at 750 °C reveals a surface with a completely different morphology than those obtained by conventional base growth of CNTs. Raman spectroscopy characterization of the surface after forceful removal of the CNT arrays (Figs. S7C and D) confirm the presence of CNTs on SiO_2. Both graphitic and RBM peaks appear in the spectrum, which could indicate that the CNTs are bonded to SiO_2 and the lingering CNTs were broken probably at their defect sites. These observations suggest that during high-temperature synthesis, carbon may react with SiO_2 to form SiC, allowing the formation of covalent bonds between the CNTs and SiO_2 surface.

In addition to investigating the influence of growth temperature, the effect of thermal reduction on the performance of the binary metal oxide catalyst was studied by varying the hydrogen exposure time. To achieve suitable growth conditions for high-yield CNT synthesis, catalyst particles must be reduced into their metallic form. Although the metallic form is a well-known catalyst that is active for CNT growth, a few studies have indicated that the metal oxide could act as a catalyst for single- and multiwall CNTs [60,61]. Flowing H_2 gas (400 sccm) for different lengths of time (0, 3, 5, and 8 min) at 720 °C before introducing the carbon precursor into the furnace, the lengths of the obtained CNTs were compared based on the reduction times. SEM images of the VA-CNTs obtained with different thermal annealing times are shown in Fig. S8. Notably, shorter (83 μm) CNTs were synthesized with no thermal reduction (0 min) (Fig. S8A). The reduction of the catalyst particles over 3 min produced the longest CNTs (254 μm, Fig. S8B), whereas a length of 246 μm was obtained with reduction times of 5 and 8 min. Raman analysis was used to understand the effect of catalyst reduction on the quality of the CNTs. The Raman spectra of the CNTs grown with different catalyst reduction times are shown in Fig. S9. The CNTs grown without catalyst reduction exhibit the poorest quality, as indicated by the low intensity of the G peak (Fig. S9A). Irrespective of the reduction time, all the CNTs grown following catalyst reduction exhibit similar quality, with a higher G peak intensity.

4. Conclusions

The AlO_x–Fe_2O_3 nanorice monolayer film, created using a wet-chemical method, provides an effective approach for the synthesis of VA-CNT on SiO_2 substrates without the need of additional Al_2O_3 catalyst support layer. These premade binary metal oxide particles, which includes both Fe_2O_3 and AlOx, enabled the growth of VA-CNTs on bare SiO_2. The resulting CNT lengths are comparable to those grown on a sputtered Al_2O_3 thin film. The presence of AlO_x in the nanorice should prevents catalyst ripening on plain SiO_2 substrate, similar to the effect of a 10 nm Al_2O_3 layer of sputtered substrates. The relative narrow distribution of binary metal oxide nanorice particles in the monolayer assembly aids in the synthesis of about 200 μm VA-CNTs, a process that is challenging with conventional drop casting or spin coating methods. By adjusting the growth temperature during the CVD reaction, the structural features, such as diameter, length, and purity can be optimized. Thermal reduction in with atomic hydrogen is crucial for converting of Fe_2O_3 to Fe, which enhances both the length and quality of the VA-CNTs. These results suggest that the AlO_x–Fe_2O_3 nanorice facilitates the synthesis of VA-CNTs via tip growth. The wet-chemistry preparation of these catalyst nanoparticles and their monolayer assembly on planar substrates offers an inexpensive and scalable method for VA-CNT synthesis.

CRediT authorship contribution statement

Abdul Hoque: Writing – original draft, Validation, Methodology,

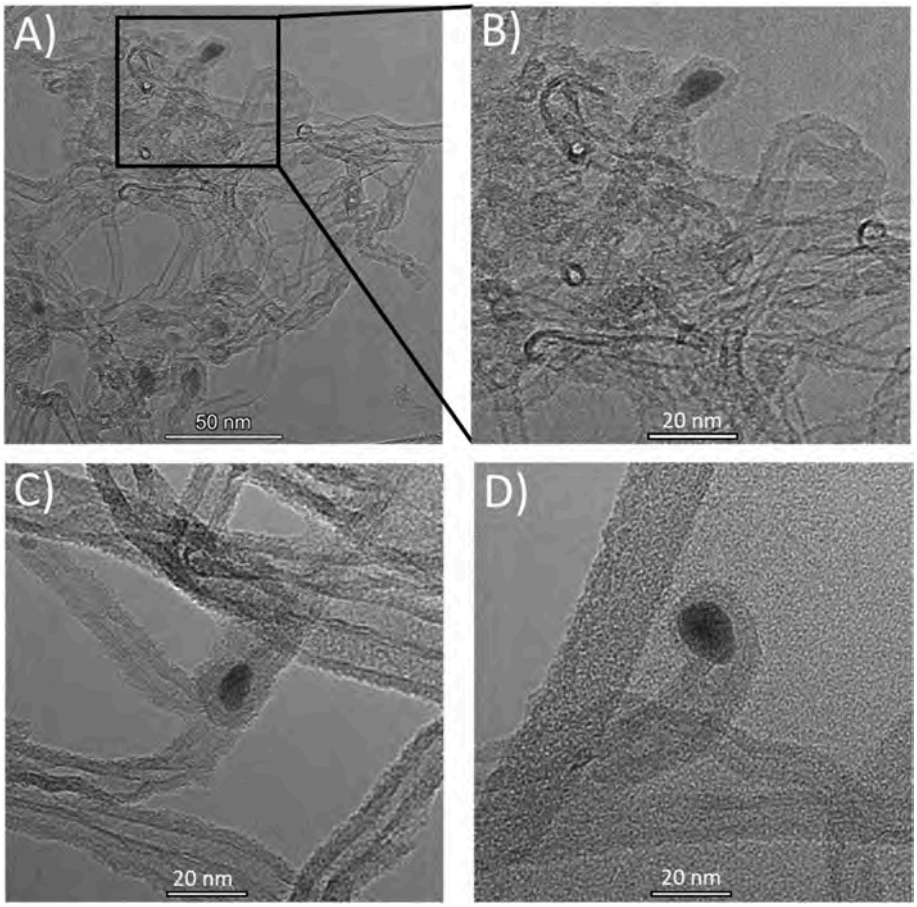

Fig. 6. TEM images of catalyst particles on the CNT tips. (A) Low-magnification and (B–D) higher magnification TEM images of catalyst particles on the tips of CNTs grown using the binary metal AlO_x–Fe_2O_3 nanorice on a SiO_2 substrate at 750 °C.

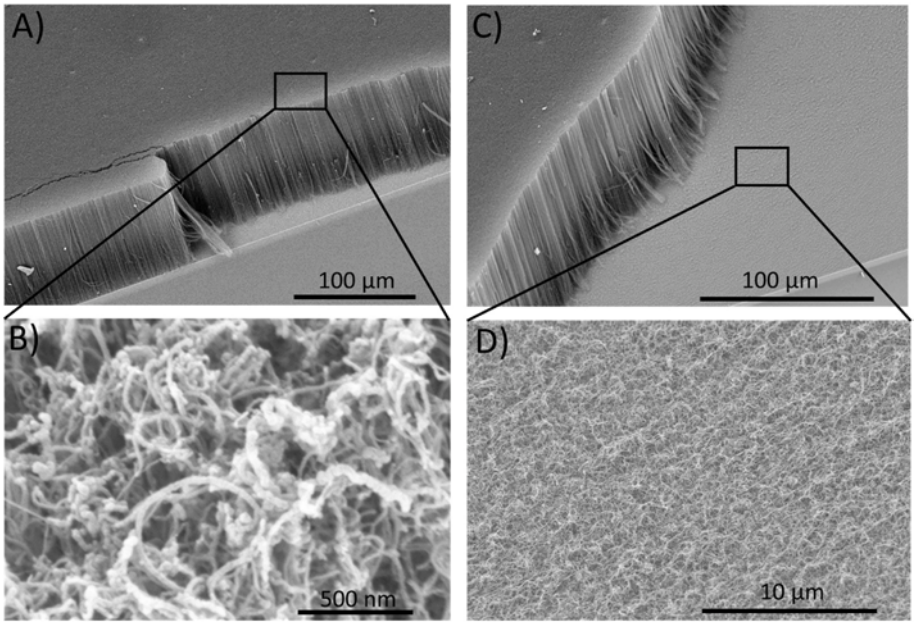

Fig. 7. SEM images of VA-CNTs grown at 750 °C. (A) SEM image of the side of the CNTs, (B) high-magnification SEM image of CNT tips with catalyst particles on top, (C) SEM image showing both the side of the CNTs and the substrate surface after forcefully removing the CNTs, and (D) high-magnification SEM image of the substrate surface showing randomly attached CNTs.

Investigation, Formal analysis, Data curation. **Chaminda P. Nawarathne:** Writing – review & editing, Investigation, Formal analysis. **Noe T. Alvarez:** Writing – review & editing, Supervision, Funding acquisition, Conceptualization.

Declaration of competing interest

The authors declare that they have no known competing financial interests or personal relationships that could have appeared to influence the work reported in this paper.

Acknowledgments

The authors are extremely grateful to grants NSF DMR 2334039 and NSF PFI-RP 2016484.

Appendix A. Supplementary data

Supplementary data to this article can be found online at https://doi.org/10.1016/j.carbon.2025.120086.

References

[1] Y. Hayashi, K.P. Selvam, M. Scholz, Rapid growth of dense and long carbon nanotube arrays and its application in spinning thread, in: M.M.a.A. Rahman, A. M. (Ed.), Carbon Nanotubes - Recent Progress, Intechopen2018.
[2] B. Dai, R. Zhou, J. Ping, Y. Ying, L. Xie, Recent advances in carbon nanotube-based biosensors for biomolecular detection, TrAC, Trends Anal. Chem. 154 (2022).
[3] R. Malik, L. Zhang, C. McConnell, M. Schott, Y.Y. Hsieh, R. Noga, N.T. Alvarez, V. Shanov, Three-dimensional, free-standing polyaniline/carbon nanotube composite-based electrode for high-performance supercapacitors, Carbon 116 (2017) 579–590.
[4] P.K. Adusei, S. Gbordzoe, S.N. Kanakaraj, Y.-Y. Hsieh, N.T. Alvarez, Y. Fang, K. Johnson, C. McConnell, V. Shanov, Fabrication and study of supercapacitor electrodes based on oxygen plasma functionalized carbon nanotube fibers, J. Energy Chem. 40 (2020) 120–131.
[5] S. Park, M. Vosguerichian, Z. Bao, A review of fabrication and applications of carbon nanotube film-based flexible electronics, Nanoscale 5 (5) (2013) 1727–1752.
[6] P. Avouris, M. Freitag, V. Perebeinos, Carbon-nanotube photonics and optoelectronics, Nat. Photonics 2 (6) (2008) 341–350.
[7] T. Maruyama, T. Okada, K.P. Sharma, T. Suzuki, T. Saida, S. Naritsuka, Y. Iizumi, T. Okazaki, S. Iijima, Vertically aligned growth of small-diameter single-walled carbon nanotubes by alcohol catalytic chemical vapor deposition with Ir catalyst, Appl. Surf. Sci. 509 (2020).
[8] D.A. Heller, S. Baik, T.E. Eurell, M.S. Strano, Single-walled carbon nanotube spectroscopy in live cells: towards long-term labels and optical sensors, Adv. Mater. 17 (23) (2005) 2793–2799.
[9] V.B. Koman, N.A. Bakh, X. Jin, F.T. Nguyen, M. Son, D. Kozawa, M.A. Lee, G. Bisker, J. Dong, M.S. Strano, A wavelength-induced frequency filtering method for fluorescent nanosensors in vivo, Nat. Nanotechnol. 17 (6) (2022) 643–652.
[10] N.T. Alvarez, P. Miller, M.R. Haase, R. Lobo, R. Malik, V. Shanov, Tailoring physical properties of carbon nanotube threads during assembly, Carbon 144 (2019) 55–62.
[11] N.T. Alvarez, P. Miller, M. Haase, N. Kienzle, L. Zhang, M.J. Schulz, V. Shanov, Carbon nanotube assembly at near-industrial natural-fiber spinning rates, Carbon 86 (2015) 350–357.
[12] B.C. Edwards, Design and deployment of a space elevator, Acta Astronaut. 47 (2000) 735–744.
[13] Y. Bai, R. Zhang, X. Ye, Z. Zhu, H. Xie, B. Shen, D. Cai, B. Liu, C. Zhang, Z. Jia, S. Zhang, X. Li, F. Wei, Carbon nanotube bundles with tensile strength over 80 GPa, Nat. Nanotechnol. 13 (7) (2018) 589–595.
[14] C. Feng, L. Jiang, Micromechanics modeling of the electrical conductivity of carbon nanotube (CNT)–polymer nanocomposites, Compos. Appl. Sci. Manuf. 47 (2013) 143–149.
[15] B.R. Lettiere, C.A.C. Chazot, K. Cui, A.J. Hart, High-density carbon nanotube forest growth on copper foil for enhanced thermal and electrochemical interfaces, ACS Appl. Nano Mater. 3 (1) (2020) 77–83.
[16] H. Na, J.H. Park, J. Hwang, J. Kim, Site-specific growth and density control of carbon nanotubes by direct deposition of catalytic nanoparticles generated by spark discharge, Nanoscale Res. Lett. 8 (1) (2013) 409.
[17] P.B. Amama, C.L. Pint, S.M. Kim, L. McJilton, K.G. Eyink, E.A. Stach, R.H. Hauge, B. Maruyama, Influence of alumina type on the evolution and activity of alumina-supported Fe catalysts in single-walled carbon nanotube carpet growth, ACS Nano 4 (2) (2010) 895–904.
[18] S.V. Bulyarskiy, A.V. Lakalin, A.A. Pavlov, A.A. Dudin, E.P. Kitsyuk, E.M. Eganova, A.P. Sirotina, A.A. Shamanaev, A model of carbon-nanotube growth-rate limitation on thin-film catalysts, Tech. Phys. Lett. 43 (4) (2017) 366–368.
[19] M. Li, M. Risa, T. Osawa, H. Sugime, S. Noda, Facile catalyst deposition using mists for fluidized-bed production of sub-millimeter-long carbon nanotubes, Carbon 167 (2020) 256–263.
[20] H. Goktas, N. Lachman, E. Kalfon-Cohen, X. Wang, S. Torosian, K.K. Gleason, B. L. Wardle, Facile growth of high-yield and -crystallinity vertically aligned carbon nanotubes via a sublimated ferric chloride catalyst precursor, Nano Futures 7 (2) (2023).
[21] Y. Inoue, K. Kakihata, Y. Hirono, T. Horie, A. Ishida, H. Mimura, One-step grown aligned bulk carbon nanotubes by chloride mediated chemical vapor deposition, Appl. Phys. Lett. 92 (21) (2008).
[22] N.T. Alvarez, F. Li, C.L. Pint, J.T. Mayo, E.Z. Fisher, J.M. Tour, V.L. Colvin, R. H. Hauge, Uniform large diameter carbon nanotubes in vertical arrays from premade near-monodisperse nanoparticles, Chem. Mater. 23 (2011) 3466–3475.
[23] S.S. Lee, C. Zhang, Z.A. Lewicka, M. Cho, J.T. Mayo, W.W. Yu, R.H. Hauge, V. L. Colvin, Control over the diameter, length, and structure of carbon nanotube carpets using aluminum ferrite and iron oxide nanocrystals as catalyst precursors, J. Phys. Chem. C 116 (18) (2012) 10287–10295.
[24] A. Hoque, A. Ullah, B.S. Guiton, N.T. Alvarez, Premade nanoparticle films for the synthesis of vertically aligned, Carbon Nanotubes, C 7 (4) (2021).
[25] S. Mosallanejad, B.Z. Dlugogorski, E.M. Kennedy, M. Stockenhuber, On the chemistry of iron oxide supported on gamma-alumina and silica catalysts, ACS Omega 3 (5) (2018) 5362–5374.
[26] H. Ohno, D. Takagi, K. Yamada, S. Chiashi, A. Tokura, Y. Homma, Growth of vertically aligned single-walled carbon nanotubes on alumina and sapphire substrates, Jpn. J. Appl. Phys. 47 (4) (2008) 1956–1960.
[27] Y. Homma, Carbon nanotube synthesis and the role of catalyst, Frontiers of graphene and carbon nanotubes (2015) 125–129. Springer.
[28] Z. Pan, H. Zhu, Z. Zhang, H.-j. Im, S. Dai, D.B. Beach, D.H. Lowndes, Patterned growth of vertically aligned carbon nanotubes on pre-patterned iron/silica substrates prepared by Sol−Gel and shadow masking, J. Phys. Chem. B 107 (6) (2003) 1338–1344.
[29] Y.J. Jung, Wei, R. Vajtai, P.M. Ajayan, Y. Homma, K. Prabhakaran, T. Ogino, Mechanism of selective growth of carbon nanotubes on SiO2/Si patterns, Nano Lett. 3 (4) (2003) 561–564.
[30] S. Honda, Y.G. Baek, K.Y. Lee, T. Ikuno, T. Kuzuoka, J.T. Ryu, S. Ohkura, M. Katayama, K. Aoki, T. Hirao, K. Oura, Synthesis of randomly oriented carbon nanotubes on SiO2 substrates by thermal chemical vapor deposition toward field electron emitters, Thin Solid Films 464–465 (2004) 290–294.
[31] Y.D. Lim, L. Hu, A.V. Avramchuck, D. Grapov, B.K. Tay, S. Aditya, J. Miao, V. Labunov, Temperature-dependent selective growth of carbon nanotubes in Si/SiO2 structures for field emitter array applications, Mater. Res. Bull. 95 (2017) 129–137.
[32] A. Kaneko, K. Yamada, R. Kumahara, H. Kato, Y. Homma, Comparative study of catalytic activity of iron and cobalt for growing carbon nanotubes on alumina and silicon oxide, J. Phys. Chem. C 116 (49) (2012) 26060–26065.
[33] N.T. Alvarez, C.E. Hamilton, C.L. Pint, A. Orbaek, J. Yao, A.L. Frosinini, A. R. Barron, J.M. Tour, R.H. Hauge, Wet catalyst-support films for production of vertically aligned carbon nanotubes, ACS Appl. Mater. Interfaces 2 (2010) 1851–1856.
[34] A. Hoque, A. Huseinov, C.P. Nawarathne, N.T. Alvarez, Synthesis of bimetallic aluminum–iron oxide nanorice, nanocubes and nanospheres, New J. Chem. 47 (30) (2023) 14249–14260.
[35] J. Park, K. An, Y. Hwang, J.G. Park, H.J. Noh, J.Y. Kim, J.H. Park, N.M. Hwang, T. Hyeon, Ultra-large-scale syntheses of monodisperse nanocrystals, Nat. Mater. 3 (12) (2004) 891–895.
[36] A. Hoque, A. Ullah, P. Joshi, B.S. Guiton, N.T. Alvarez, Spherical aluminum oxide nanoparticle synthesis and monolayer film assembly, J. Mater. Sci. 58 (17) (2023) 7287–7302.
[37] O. Yildirim, T. Gang, S. Kinge, D.N. Reinhoudt, D.H. Blank, W.G. van der Wiel, G. Rijnders, J. Huskens, Monolayer-directed assembly and magnetic properties of FePt nanoparticles on patterned aluminum oxide, Int. J. Mol. Sci. 11 (3) (2010) 1162–1179.
[38] R.G. Acres, A.V. Ellis, J. Alvino, C.E. Lenahan, D.A. Khodakov, G.F. Metha, G. G. Andersson, Molecular structure of 3-aminopropyltriethoxysilane layers formed on silanol-terminated silicon surfaces, J. Phys. Chem. C 116 (10) (2012) 6289–6297.
[39] C. Queffelec, M. Petit, P. Janvier, D.A. Knight, B. Bujoli, Surface modification using phosphonic acids and esters, Chem. Rev. 112 (7) (2012) 3777–3807.
[40] T. Yamashita, P. Hayes, Analysis of XPS spectra of Fe2+ and Fe3+ ions in oxide materials, Appl. Surf. Sci. 254 (8) (2008) 2441–2449.
[41] T. Liu, J. Qin, J. Wang, J. Li, On the tribological properties of RGO–MoS2 composites surface modified by oleic acid, Tribol. Lett. 70 (1) (2022).
[42] Q. Liu, X. Shi, Q. Jiang, R. Li, S. Zhong, R. Zhang, Growth mechanism and kinetics of vertically aligned carbon nanotube arrays, EcoMat 3 (4) (2021).
[43] A.R. Bogdanova, D.V. Krasnikov, E.M. Khabushev, B.J. Ramirez, Y.E. Matyushkin, A.G. Nasibulin, Role of hydrogen in ethylene-based synthesis of single-walled carbon nanotubes, Nanomaterials 13 (9) (2023).
[44] T. Tsuji, J. Kim, H. Sakakita, Y. Shimizu, G. Chen, K. Hata, D.N. Futaba, S. Sakurai, Role of hydrogen in catalyst activation for plasma-based synthesis of carbon nanotubes, ACS Omega 6 (29) (2021) 18763–18769.
[45] A. Szabo, P. Andricevic, Z. Papa, T. Gyulavari, K. Nemeth, E. Horvath, L. Forro, K. Hernadi, Growth of CNT forests on titanium based layers, detailed study of catalysts, Front. Chem. 6 (2018) 593.
[46] L. Qiu, F. Ding, Contact-Induced phase separation of alloy catalyst to promote carbon nanotube growth, Phys. Rev. Lett. 123 (25) (2019) 256101.

[47] Ç. Öncel, Y. Yürüm, Carbon nanotube synthesis via the catalytic CVD method: a review on the effect of reaction parameters, Fullerenes, Nanotub. Carbon Nanostruct. 14 (1) (2006) 17–37.
[48] C. Laurent, E. Flahaut, A. Peigney, The weight and density of carbon nanotubes versus the number of walls and diameter, Carbon 48 (2010) 2989–2999.
[49] A. Jorio, R. Saito, Raman spectroscopy for carbon nanotube applications, J. Appl. Phys. 129 (2) (2021).
[50] P. Puech, M. Kandara, G. Paredes, L. Moulin, E. Weiss-Hortala, A. Kundu, N. Ratel-Ramond, J.-M. Plewa, R. Pellenq, M. Monthioux, Analyzing the Raman spectra of graphenic carbon materials from kerogens to nanotubes: what type of information can Be extracted from defect bands?, C 5 (4) (2019).
[51] S.D.M. Brown, A. Jorio, M.S. Dresselhaus, G. Dresselhaus, Observations of theD-band feature in the Raman spectra of carbon nanotubes, Phys. Rev. B 64 (7) (2001).
[52] Q.N. Pham, L.S. Larkin, C.C. Lisboa, C.B. Saltonstall, L. Qiu, J.D. Schuler, T. J. Rupert, P.M. Norris, Effect of growth temperature on the synthesis of carbon nanotube arrays and amorphous carbon for thermal applications, Phys. Status Solidi 214 (7) (2017).
[53] Y. Park, K.P.S.S. Hembram, R. Yoo, B. Jang, W. Lee, S.-G. Lee, J.-G. Kim, Y.-I. Kim, D.J. Moon, J.-K. Lee, J.-K. Lee, Reinterpretation of single-wall carbon nanotubes by Raman spectroscopy, J. Phys. Chem. C 123 (22) (2019) 14003–14009.
[54] K. Cui, A. Kumamoto, R. Xiang, H. An, B. Wang, T. Inoue, S. Chiashi, Y. Ikuhara, S. Maruyama, Synthesis of subnanometer-diameter vertically aligned single-walled carbon nanotubes with copper-anchored cobalt catalysts, Nanoscale 8 (3) (2016) 1608–1617.
[55] T. Sato, K. Nakamura, S. Takagiwa, M. Kushida, Controlling the morphology of Vertically-aligned carbon nanotubes using Langmuir-Blodgett deposited CoFe2O4, Fe3O4, and Fe nanoparticles with palmitic acid, Thin Solid Films 616 (2016) 662–672.
[56] A. Baliyan, Y. Nakajima, T. Fukuda, T. Uchida, T. Hanajiri, T. Maekawa, Synthesis of an ultradense forest of vertically aligned triple-walled carbon nanotubes of uniform diameter and length using hollow catalytic nanoparticles, J. Am. Chem. Soc. 136 (3) (2014) 1047–1053.
[57] J.D. Beard, J. Stringer, O.R. Ghita, P.J. Smith, High yield growth of patterned vertically aligned carbon nanotubes using inkjet-printed catalyst, ACS Appl. Mater. Interfaces 5 (19) (2013) 9785–9790.
[58] N.T. Alvarez, A. Orbaek, A.R. Barron, J.M. Tour, R.H. Hauge, Dendrimer-assisted self-assembled monolayer of iron nanoparticles for vertical array carbon nanotube growth, ACS Appl. Mater. Interfaces 2 (1) (2010) 15–18.
[59] I.K. Song, Y.S. Cho, G.S. Choi, J.B. Park, D.J. Kim, The growth mode change in carbon nanotube synthesis in plasma-enhanced chemical vapor deposition, Diam. Relat. Mater. 13 (4–8) (2004) 1210–1213.
[60] S.A. Steiner 3rd, T.F. Baumann, B.C. Bayer, R. Blume, M.A. Worsley, W. J. MoberlyChan, E.L. Shaw, R. Schlogl, A.J. Hart, S. Hofmann, B.L. Wardle, Nanoscale zirconia as a nonmetallic catalyst for graphitization of carbon and growth of single- and multiwall carbon nanotubes, J. Am. Chem. Soc. 131 (34) (2009) 12144–12154.
[61] C.T. Wirth, B.C. Bayer, A.D. Gamalski, S. Esconjauregui, R.S. Weatherup, C. Ducati, C. Baehtz, J. Robertson, S. Hofmann, The phase of iron catalyst nanoparticles during carbon nanotube growth, Chem. Mater. 24 (24) (2012) 4633–4640.